Measurement Report: Elevated atmospheric ammonia may promote the particle pH and HONO formation: Insights from the COVID-19 pandemic

Xinyuan Zhang[1,2], Lingling Wang[3], Nan Wang[3], Shuangliang Ma[3], Shenbo Wang[2,4] *, Ruiqin Zhang[2,4**], Dong Zhang[1,2], Mingkai Wang[2,4], Hongyu Zhang[1,2].

[1] College of Chemistry, Zhengzhou University, Zhengzhou, 450000, China

[2] Research Institute of Environmental Sciences, Zhengzhou University, Zhengzhou 450000, China

[3] Henan Provincial Ecological Environment Monitoring and Safety Center, Zhengzhou, 450000, China

[4] School of Ecology and Environment, Zhengzhou University, Zhengzhou, 450000, China

Correspondence: Shenbo Wang (shbwang@zzu.edu.cn) and Ruiqin Zhang (rqzhang@zzu.edu.cn)

Abstract

HONO plays a crucial role as a precursor to OH radicals in the tropospheric atmosphere. The incongruity between HONO concentration and NO_x emissions during the COVID-19 pandemic remains puzzling. Here, we show evidence from field observations of ten sites in China that there was a noticeable increase in NH_3 concentrations during the COVID-19 pandemic. In addition to the meteorological conditions, the significant decrease in sulfate and nitrate concentrations enhanced the portioning of NH_4^+ to NH_3. Sensitivity analysis indicated that the decrease in anion concentrations (especially sulfate and nitrate) and the increase in cation concentrations during the COVID-19 pandemic led to an increase in particle pH. In other words, the excess ammonia determined the promoting pH. The calculation of reaction rates indicates that during the epidemic, the increase in pH may promote the generation of HONO by facilitating redox reactions, which highlights the importance of coordinating the control of SO_2, NO_x, and NH_3 emissions.

Keywords: Ammonia, HONO, Gas-particle portioning, Acidity, COVID-19 pandemic

1. Introduction

Nitrous acid (HONO) is a critical precursor of hydroxyl radical (OH), contributing to more than 60% of OH production (Alicke, 2003;Platt et al., 1980;Kleffmann et al., 2005). The OH can react with carbon monoxide, nitrogen oxides (NO_x), sulfur dioxide (SO_2), and volatile organic compounds to produce secondary pollutants such as ozone (O_3) and $PM_{2.5}$ (particulate matter with an aerodynamic diameter less than or equal to 2.5 μm), thereby affecting air quality, human health, and global climate change (Li et al., 2021a;Wang et al., 2023b;Lu et al., 2018)

High concentrations of HONO are present in urban daytime atmospheres, and exploring its sources has become a hot and challenging topic in the field of atmospheric chemistry (Jiang et al., 2022;Xu et al., 2019). Various sources of atmospheric HONO have been identified, including combustion processes (e.g., vehicle emissions) (Kramer et al., 2020;Liao et al., 2021a;Li et al., 2021b), direct emissions from soil (Su and Zhang, 2011;Oswald et al., 2013;Meusel et al., 2018), homogeneous reactions between NO and OH radicals (Pagsberg, 1997;Atkinson and Rossi, 2004), heterogeneous reactions of NO_2 on aerosols and ground surfaces (Zhang et al., 2020a;McFall et al., 2018;Liu et al., 2014;Liu et al., 2020a), and photolysis of nitrate (Spataro and Ianniello, 2014;Scharko et al., 2014;Romer et al., 2018;Ye et al., 2017;Shi et al., 2021). During the pandemic control periods, there was a substantial reduction in vehicle traffic flow and industrial emissions, leading to a decrease of more than 60% in NO_x emissions in eastern China (Huang et al., 2021a). It was initially expected that the concentration of HONO would also decrease proportionally. However, Liu et al. (2020b) observed that the decrease in

57 HONO concentration during the pandemic period was only 31% (from 1.5 ppb to 0.9

58 ppb), which was significantly lower than the reductions in NO (62%, from 26.3 to 4.2

59 ppb) and NO_2 (36%, from 15.5 to 6.2 ppb). Furthermore, the observed concentrations

60 of HONO during the COVID-19 pandemic in 2020 were higher than those during the

61 corresponding period in 2021 in Beijing (Luo et al., 2023). These findings suggest the

62 existence of a considerable unknown source of HONO during the COVID-19 pandemic

63 period.

64   Ammonia (NH_3) is a primary alkaline gas in the atmosphere, capable of influencing

65 the pH level of particulate matter and plays a crucial role in the atmospheric nitrogen

66 cycle (Gu et al., 2022;Xu et al., 2020;Gong et al., 2011). Several studies have indicated

67 that NH_3 can promote the formation of HONO by promoting the hydrolysis of NO_2 (Xu

68 et al., 2019) or the redox reaction of NO_2 with SO_2 (Liu et al., 2023). Moreover,

69 previous studies have reported that NH_3 concentrations in the atmosphere, particularly

70 in rural areas, significantly increased during the pandemic (Xu et al., 2022).

71 Consequently, the rise in NH_3 may contribute to the enhanced formation of HONO

72 (Huang et al., 2021a). Unfortunately, there is currently a lack of research on the

73 relationship between enhanced NH_3 and HONO during the COVID-19 pandemic period.

74   To address this, online observational data on the chemical composition of $PM_{2.5}$,

75 gaseous pollutants, and meteorological conditions at ten sites in China before and

76 during the COVID-19 pandemic period were analyzed to investigate the variation in

77 NH_3 concentrations and particle pH, and explore the promoting effect of increased pH

78 values on HONO formation.

2. Materials and methods

2.1 Observation sites

Online measurements were conducted at four urban and six rural sites in Henan Province, China from January 1 to February 29, 2020, including Sanmenxia (U-SMX), Zhoukou (U-ZK), Zhumadian (U-ZMD), and Xinyang (U-XY), as well as rural locations including Anyang (R-AY), Xinxiang (R-XX), Jiaozuo (R-JZ), Shangqiu (R-SQ), Nanyang (R-NY), and Puyang (R-PY). Descriptions and the spatial distribution of these ten sites can be found in Table S1 and Fig. S1.

2.2 Measurements

The aerosol and gas monitor (MARGA, Metrohm, Switzerland) was used to analyze the hourly water-soluble ions (Na^+, NH_4^+, K^+, Mg^{2+}, Ca^{2+}, Cl^-, NO_3^-, and SO_4^{2-}) in $PM_{2.5}$, as well as gaseous species (NH_3, HNO_3, HCl, and $HONO$) at ten sampling sites. The MARGA instrument is widely used (Chen et al., 2017;Stieger et al., 2019;Twigg et al., 2022). A detailed description of the instrument and QA/QC can be found in Text S1. In brief, the atmospheric sample passes through a $PM_{2.5}$ cut-off head, and both particles and gases enter a wet rotating dissolution device for diffusion. Subsequently, the particles in the sample undergo hygroscopic growth and condensation in an aerosol supersaturated vapor generator, followed by collection and ion chromatographic analysis. The gases in the sample are oxidized by H_2O_2 in the dissolution device, absorbed into a liquid solvent, and then entered the gas sample collection chamber for

99   ion chromatographic quantification. The range of minimum detection limits for water-

100   soluble ions was between 0.002 μg/m^3 (Cl$^-$) to 0.081 μg/m^3 (NH$_4^+$). Uncertainties of 20%

101   are assumed for the detection of NH$_3$ and NH$_4^+$, while uncertainties of 10% are assumed

102   for other components (Wang et al., 2020;Wang et al., 2022). In addition, a detailed

103   description of HONO measurement using this system can be found in Text S2. Overall,

104   the limit of detection for HONO was 4 pptv and the uncertainty was estimated to be ±

105   20%.

106   The data for NO$_2$ and SO$_2$ were obtained from a series of instruments provided by

107   Thermo Fisher Scientific (USA). The hourly concentrations of organic carbon (OC) in

108   PM$_{2.5}$ were analyzed using a carbon analyzer (Model 4, Sunset Laboratory., USA).

109   Detailed descriptions of the NO$_2$, SO$_2$, and carbon analyzers can be found in Text S3.

110   The smart weather stations (LUFFTWS500, Sutron, Germany) were utilized for

111   synchronized observation of meteorological parameters including pressure,

112   temperature (T), and relative humidity (RH).

113   **2.3 Data analysis.**

114   **2.3.1 pH prediction.**

115   The thermodynamic model ISORROPIA-II was used to estimate the pH value of the

116   particles (Fountoukis, 2007) by inputting RH, T, K$^+$, Ca^{2+}, Mg^{2+}, total ammonia

117   ($TNH_x = 17 \times (\frac{[NH_4^+]}{18} + \frac{[NH_3]}{17})$), total sulfuric acid (TH$_2$SO$_4$, SO$_4^{2-}$), total sodium

118   (TNa, Na$^+$), total chlorine (TCl, Cl$^-$), and total nitrate (TNO$_3$ = NO$_3^-$ + HNO$_3$). The

119   model has two calculation modes: the forward mode and reverse mode, and the aerosol

120   dissolution systems can be set to simulate a metastable state (aqueous phase) or stable

121   state (aqueous and solid phase). Studies have shown that the forward mode is less

122   affected by instrument measurement errors than the reverse mode (Ding et al.,

123   2019;Song et al., 2018). Additionally, the minimum average RH of about 55% was

124   recorded during the sampling period at the ten sites. Thus, ISORROPIA-II was run in

125   the forward model for the aerosol system in the metastable condition and only used data

126   with RH $\geq$ 30% for simulation accuracy (Ding et al., 2019;Song et al., 2018). The

127   ISORROPIA model calculated the particle hydrate ion concentration per volume of air

128   (H_{air}^{+}) and aerosol water associated with inorganic matter (AWC_{inorg}). The pH value

129   was calculated using the following equation (Bougiatioti et al., 2016):

130
$$pH = -\log_{10} H_{aq}^{+} = -\log_{10} \frac{1000 H_{air}^{+}}{AWC_{inorg} + AWC_{org}} \qquad (2.1)$$

131   where the modeled concentrations for AWC_{inorg} and H_{air}^{+} are $\mu g/m^3$, and AWC_{org} is the

132   particle water associated with the organic matters predicted using the following method:

133
$$AWC_{org} = \frac{m_s}{\rho_s} \frac{k_{org}}{\left(\dfrac{1}{RH} - 1 \right)} \qquad (2.2)$$

134   where m_s is the mass concentration of organic matter (OM = OC $\times$ f). The f is the

135   conversion factor of OC, which is dependent on the extent of OM oxidation and

136   secondary organic aerosol formation (Chow et al., 2015). Studies on the ratio of

137   OM/OC in fourteen cities in China suggested that the mean value of f was 1.59 ± 0.18

138   during the winter season in Northern China (Xing et al., 2013), and thus we adopted 1.6

139   as the f in this study. k_{org} is the organic hygroscopicity parameter and depends on organic

140   functionality, water solubility, molecular weight, and oxidation level. Han et al. (2022)

141   have reported that the k_{org} generally increased with O: C ratios, with a range of 0–0.3

142   for 23 organics, including carboxylic acids, amino acids, sugars, and alcohols. Gunthe

143   et al. (2011) estimated a $k_{org} = 0.06 \pm 0.01$ for the effective average hygroscopicity of

144   the non-refractory organic particulate matter in the aerosols in Beijing. Our previous

145   study has estimated that the uncertainties of k_{org} value (0.06) for pH in the range of 0–

146   0.3 only lead to –1–3% errors, which can be neglected (Wang et al., 2023a). Therefore,

147   the value of 0.06 was selected in this paper. ρ_s is the organic density, which was chosen

148   to be 1.35 g/cm^3 following previous studies (Table S2).

2.3.2 The sources of HONO

150   The sources of HONO include direct emission (P_{emi}), the homogeneous reaction of

151   NO and •OH (P_{OH+NO}), the heterogeneous reaction of NO_2 on the ground (P_{ground}) and

152   aerosol ($P_{aerosol}$), the photo-enhanced heterogeneous reaction of NO_2 on the ground

153   ($P_{ground+hv}$) and aerosol ($P_{aerosol+hv}$), and nitrate photolysis ($P_{nitrate}$). The detailed

154   calculation method is described in the Supplementary Material (Text S4, Table S3, Figs.

155   S2 and S3).

156   Soil emission has been demonstrated to be a major source of HONO, which is affected

157   by temperature to some extent (Liu et al., 2020c;Liu et al., 2020b). However, during the

158   sampling periods, there was no significant positive correlation between HONO

159   concentration and temperature (Fig. S4). In addition, temperatures did not exceed 10°C,

160   under which the soil HONO emission rate is generally considered to be zero (Zhang et

al., 2023). Furthermore, the equilibrium gas-phase concentration over an aqueous

solution of nitrous acid, [HONO]*, a key parameter controlling the exchange of HONO

between the gas and aqueous phase in soil, is calculated according to Su et al.(2011).

The results indicate that the temperature difference between PC and DC periods only

led to approximately a 0.01% concentration change. On the other hand, studies on the

sources of HONO in the North China Plain of China during winter consistently showed

that soil HONO emissions contribute around 1% (Liu et al., 2020c;Liu et al.,

2020b;Zhang et al., 2023). Therefore, this study does not consider soil HONO

emissions.

2.3.3 Redox reaction of NO_2 with SO_2.

The redox reaction of NO_2 with SO_2 (R_1) is considered a crucial potential source of

high concentrations of HONO in Northern China (Cheng et al., 2019;Wang et al., 2016):

$$S(IV) + 2NO_2 + H_2O \rightarrow S(VI) + 2H^+ + 2NO_2^- \tag{R_1}$$

the rate expression for reaction (R_1) was estimated to:

$$d[S(VI)] / dt = k_1[NO_2][S(VI)], \tag{2.3}$$

the rate constant k_1 value is pH dependent, e.g., for pH, 5, $k_1 = (1.4\times10^5 + 1.24\times10^7)/2$

$M^{-1} s^{-1}$. For k_1 values under other pH conditions and other related information, please

refer to Text S5, Table S4, and Table S5.

3. Results and discussion

3.1 Variations of NH$_3$, NH$_4^+$ and TNH$_x$.

The temporal variations of NH$_3$, NH$_4^+$, and TNH$_x$ at 10 sampling sites in the pre-COVID-19 pandemic period (PC, January 1 to 23, 2020) and during the COVID-19 pandemic period (DC, January 24 to February 29, 2020) are presented in Fig. 1, with their average concentration listed in Table 1. In general, rural sites exhibited higher concentrations of NH$_3$, NH$_4^+$, and TNH$_x$ compared to urban sites, except for the R-NY site. This finding is consistent with previous studies conducted in Zhengzhou (Wang et al., 2020), Shanghai (Chang et al., 2019), and Quzhou (Feng et al., 2022), owing to the intense agricultural ammonia emissions. The highest concentrations of NH$_3$ and TNH$_x$ were recorded at site R-JZ, with average values of 25.3 ± 11.5 and 40.8 ± 20.1 μg/m^3, respectively. Site R-AY had the highest NH$_4^+$ concentration, measuring 19.3 ± 12.9 μg/m^3. Note that the current study area exhibited higher NH$_3$ levels compared to other regions (Table S6), which probably was attributed to the highest NH$_3$ emissions of Henan Province in China, primarily from nitrogen fertilizer application and livestock farming (Wang et al., 2018;Ma, 2020).

Compared to the PC, NH$_3$ concentrations increased in the DC at all sites. Notably, rural sites experienced more significant increases in NH$_3$ concentrations than urban sites, which was similar to the trend in Shanghai (Xu et al., 2022). The largest increases in NH$_3$ concentrations were observed at R-SQ (71%, 7.3 μg/m^3) and U-ZK (37%, 4.8 μg/m^3) for rural and urban sites, respectively. In contrast, the concentrations of NH$_4^+$

200 and TNH$_x$ decreased in the DC with the largest reduction at rural site R-PY (51%, 12.9

201 µg/m^3) and urban site U-ZMD (48%, 9.3 µg/m^3). Regarding TNH$_x$, rural sites exhibited

202 larger reductions, with site R-SQ experiencing the largest decrease of 37% (4.7 µg/m^3).

203   Figure 2 illustrates the spatial distribution and the diurnal variation of NH$_3$

204 concentrations at the ten sites before and during the pandemic. NH$_3$ concentrations in

205 most sites exhibited an unimodal trend in PC that NH$_3$ concentrations gradually

206 increased after sunrise, reaching a peak around noon (11:00–12:00), and then decreased

207 to a valley around 16:00–17:00. This diurnal pattern is similar to NH$_3$ variations

208 observed in urban areas of Houston, USA, as a result of the natural emissions from

209 vegetation and soil during photosynthesis (Gong et al., 2011). However, other studies

210 have recorded a significant NH$_3$ peak during the early morning of 8:00–10:00 (Ellis et

211 al., 2011;Meng et al., 2018;Gu et al., 2022), suggesting the influence of vehicle

212 emissions (Gong et al., 2011;Gu et al., 2022), residual NH$_3$ mixing, soil or plant

213 emissions (Ellis et al., 2011), and dew volatilization (Wentworth et al., 2016;Huang et

214 al., 2021b). Therefore, the NH$_3$ in urban and rural areas of this study was probably less

215 affected by NH$_3$ emissions from vehicles, different from the recent studies in megacities

216 of China (e.g., Beijing and Shanghai) (Gu et al., 2022;Wu et al., 2023;Zhang et al.,

217 2020b). In addition to the transport from agricultural emissions, urban NH$_3$ in this

218 region might also originate from other non-agricultural sources, such as wastewater

219 treatment, coal combustion, household waste, urban green spaces, and human

220 excrement (Chang et al., 2019).

221   During the COVID-19 pandemic, the diurnal variation of NH$_3$ in both urban and rural

222   sites still maintained an unimodal distribution. The peak values in urban sites remained

223   consistent with PC levels, further demonstrating that the influence of vehicles on NH_3

224   in urban areas was limited. Notably, the peak time of NH_3 in rural sites shifted 1–2 hours

225   earlier compared to the trend in PC. Ammonia in rural areas primarily originates from

226   nitrogen fertilizer application, livestock, and poultry breeding (Feng et al., 2022;Meng

227   et al., 2018), which are significantly influenced by T and RH (Liu et al., 2023). Table

228   S7 and Fig. S5 reveal that there was an increased T and a decreased RH at rural sites in

229   the DC than the PC, which could accelerate the evaporation of NH_3 and thus potentially

230   lead to earlier peak NH_3 concentrations.

231   **3.2 Gas-to-particle conversion of NH_3**

232   The increased NH_3 accompanying decreased NH_4^+ in the DC suggests that the gas-

233   particle partition of NH_3/ NH_4^+ may determine the elevated NH_3 concentrations.

234   Meteorological parameters, including RH and T, play a crucial role in the gas-particle

235   partitioning of NH_3 (Liu et al., 2023;Xu et al., 2020). Therefore, the higher T and lower

236   RH in the DC (Table S7 and Fig. S5) favored the conversion of NH_4^+ to NH_3, resulting

237   in a decrease in $\varepsilon(NH_4^+)$ ($[NH_4^+]/([NH_3] + [NH_4^+])$) compared to those in the PC (Table

238   S7).

239   NH_3 primarily enters particles to neutralize acidic ions (Wang et al., 2020;Xu et al.,

240   2020;Liu et al., 2017;Ye et al., 2011;Wells, 1998). Accordingly, the concentrations of

241   required ammonia (Required-NH_x) and excess ammonia (Excess-NH_x) were calculated

242   based on the acidic substances as follows (Wang et al., 2020):

$$\text{Required-NH}_x = 17 \times (\frac{[\text{SO}_4^{2-}]}{48} + \frac{[\text{NO}_3^-]}{63} + \frac{[\text{Cl}^-]}{35.5} + \frac{[\text{HNO}_3]}{64} + \frac{[\text{HCl}]}{36.5})$$
$$- 17 \times (\frac{[\text{Na}^+]}{23} + \frac{[\text{K}^+]}{39} + \frac{[\text{Ca}^{2+}]}{20} + \frac{[\text{Mg}^{2+}]}{12}) \tag{3.1}$$

243

$$\text{Excess-NH}_x = \text{TNH}_x - \text{Required-NH}_x \tag{3.2}$$

244

245 where [W] represents the concentration of the substance ($\mu g/m^3$). The significant linear

246 fitting (R^2 is greater than 0.96, and the slope is close to 1) in Fig. S6 demonstrates that

247 the anions and cations at each site were close to the equilibrium state. Therefore, the

248 organic acids in $PM_{2.5}$ may have less effect on NH_3 and NH_4^+ and were not considered

249 in Formula 3.1.

250   As shown in Fig. 3 and Table S8, compared to those in the PC, the concentration of

251 Required-NH_x in the DC significantly decreased (ranging from 37% at site R-JZ to 58%

252 at site R-PY), while the concentration of Excess-NH_x increased (ranging from 9% at

253 site R-AY to 78% at site R-SQ). The reduction in the concentrations of sulfate and

254 nitrate (Fig. S7) was responsible for the decrease in the concentration of Required-NH_x.

255 To sum up, in addition to meteorological conditions, the substantial reduction in

256 anthropogenic emissions of SO_2, NO_x, and other pollutants in the DC had led to a

257 decrease in acidic substances (e.g., sulfate and nitrate) in particles, in turn, resulting in

258 more gas-phase NH_3 concentration remaining in the atmosphere.

259 **3.3 Particle pH before and during COVID-19**

260   Diurnal patterns of particle pH in PC and DC at ten sites are summarized in Fig. 4

261 with their average values listed in Table S9. $PM_{2.5}$ shows consistent moderate acidity,

262 with mean values in the range of 4.2–5.1, which were close to the values in previous

263   studies (Table S9). Compared to the PC, the particle pH at ten sites increased obviously

264   in the DC, with the highest increase of 0.5 (U-ZK) and 0.3 (R-PY) at urban and rural

265   sites, respectively, which were the subject of an in-depth discussion in the following

266   text.

267   To explore the dominant factors that determine the local particle pH level and result

268   in the high pH during the DC, sensitivity tests of pH to chemical species (i.e., TNH_x,

269   TH_2SO_4, TNO_3, TCl, TNa, K^+, Ca^{2+}, and Mg^{2+}) and meteorological parameters (i.e., T

270   and RH) were performed. A given range for a variable (i.e., TNH_x) with corresponding

271   average values of other parameters (i.e., TH_2SO_4, TNO_3, TCl, TNa, K^+, Ca^{2+}, Mg^{2+}, T,

272   and RH) was input into the model and simulated to compare its effects on pH. As shown

273   in Fig. S8, pH increases with the cation concentrations (i.e., TNH_x, Na^+, K^+, Ca^{2+}, and

274   Mg^{2+}) increasing as well as the anion concentrations (i.e., TH_2SO_4, TNO_3, and Cl^-), T

275   and RH decreasing. According to the average values of input data during PC (Blue line

276   in Fig. S8) and DC (Red line in Fig. S8) at U-ZK and R-PY sites respectively, the

277   changes in pH (ΔpH in Fig. 5) indicate that the decrease in TNH_x concentration and the

278   increase in T in DC led to a decrease in pH values (ΔpH: 0.09 at U-ZK and 0.08 at R-

279   PY sites) compared to PC. However, this effect was outweighed by the decrease in

280   TH_2SO_4 (ΔpH: 0.07 and 0.8 at U-ZK and R-PY sites, respectively) and TNO_3 (ΔpH:

281   0.05 and 0.4 at U-ZK and R-PY sites, respectively) concentrations as well as the

282   increase in K^+ (ΔpH: 0.03 at U-ZK and 0.2 at R-PY site) and Mg^{2+} (ΔpH: 0.01 at U-ZK

283   and 0.04 at R-PY site) concentrations in the DC, and resulting in an overall increase in

284   pH values in the DC. Furthermore, the relationship between particle pH with the

285   concentrations of Required-NH$_x$, and Excess-NH$_x$, which considers all chemical

286   components, is investigated to examine the dominant factor on the increasing pH in DC.

287   As shown in Fig. 6, the higher Excess-NH$_x$ concentrations in the DC led to higher

288   increases in pH values (ΔpH: 1 at U-ZK and 0.5 at R-PY site) than those in PC (ΔpH:

289   0.3 at U-ZK and 0.2 at R-PY site), thus Excess-NH$_x$ concentrations may be the key

290   factor in promoting the pH values.

291   **3.4 The influence of pH on HONO.**

292   The observed HONO concentrations decreased by 18% and 54% at U-ZK (0.8 ppb)

293   and R-PY (0.9 ppb) sites in the DC, respectively, compared to those (1.0 and 2.2 ppb)

294   in the PC. Moreover, all the known HONO production sources rates including P$_{emi}$, P$_{OH}$

295    $_{+ NO}$, P$_{ground}$, P$_{ground+hv}$, P$_{aerosol}$, P$_{aerosol+hv}$, and P$_{nitrate}$ (Fig. 7, Fig S9 and S10) show a

296   decreasing trend from PC to DC, with the total reductions of 38% (from 30% to 45%

297   in the scenario with the minimum and maximum uncertainty, respectively) and 79%

298   (from 77% to 82% in the scenario with the minimum and maximum uncertainty,

299   respectively) for U-ZK and R-PY, respectively. At the U-ZK, P$_{ground+hv}$ decreased the

300   most (84%), while at the R-PY, P$_{nitrate}$ had the largest decrease about 85%, which was

301   speculated to be related to the decrease of NO$_x$ and NO$_3^-$ concentration in DC. Note that

302   the reduction rates in the overall known source and almost individual sources were

303   greater than the reduction rates in HONO concentrations (Figs. 7 and 8), thus we

304   hypothesized that there should be other sources capable of promoting HONO

305   production.

306   There were positive correlations between HONO with SO$_2$, Excess-NH$_x$, SO$_4^{2-}$, and

307   pH (Fig. S12) indicating that the R$_1$ reaction might form an amount of HONO and

308   contribute to less reduction in the observed HONO concentrations. Considering that R$_1$

309   mainly reacts in the liquid phase, the calculated reaction rates of R$_1$ under the conditions

310 of RH > 60% in the PC and DC periods are illustrated in Figs. 8 and S12. Despite the

311 decrease in NO_2 and SO_2 concentrations in the DC, the increase in particle pH,

312 increasing HSO_3^- concentration in the aqueous phase, promoted the R_1 reaction rates by

313 58% and 59% at U-ZK and R-PY (Figure 8), respectively. Consequently, the enhanced

314 R_1 reaction might prevent a large decrease in HONO (18% at U-ZK and 53% at R-PY)

315 under the conditions of a significant reduction in vehicle emissions and a decline of 66%

316 and 69% in NO_2 concentrations at U-ZK and R-PY, respectively.

3.5 Uncertainty

318 According to sensitivity tests of pH (Fig. S8) and R_1 (Fig. S12), pH increases with

319 the concentrations of cations (TNH_x, TNa, K^+, Ca^{2+}, and Mg^{2+}) and OC increasing as

320 well as anions (TH_2SO_4, TNO_3, and Cl^-) concentrations, T, and RH decreasing. R_1

321 reaction rate increases with the concentrations of AWC, NO_2, SO_2, pH, and pressure,

322 while increasing as well as T decreasing. Therefore, two extreme scenarios (i.e., the

323 maximum and minimum rate scenarios) were evaluated to estimate the uncertainty of

324 pH, and R_1 based on the measurement uncertainties at the U-ZK and R-PY sites. Figure

325 S13 suggests that the two extreme scenarios can lead to –10–7% and –71–125%

326 uncertainties at the U-ZK site and –10–7% and –78–123% uncertainties at the R-PY

327 site for pH and R_1, respectively. Even considering the above uncertainty in Fig. 8, it can

328 still be observed that during the DC period, the decrease in HONO was less than that

329 of NO_2, and the rate of the R_1 reaction increased.

330 Considering the conclusions of this study are based solely on observational data,

331 there are certain limitations. For example, only the changes in the R_1 reaction of $PM_{2.5}$

332 were calculated, without considering variations in components, pH values, and R_1

333 reaction rates of coarse particles. Additionally, although this study selected scenarios

334 with RH > 60% to calculate the R_1 reaction to ensure the presence of a liquid phase, it

335 is evident that this approach overlooks some R_1 reactions. Furthermore, due to

336 thermodynamic model calculations of pH values, changes in the mixed state of particle

337 components, and the omission of organic acids, alongside the absence of gaseous HNO_3

338 and HCl in this study, these factors may lead to inaccuracies in pH value simulations

339 and uncertainty in R_1 calculations(Pye et al., 2020;Haskins et al., 2018;Nah et al., 2018).

340 Therefore, there is a certain degree of uncertainty in the conclusions regarding the

341 growth of R_1 reactions in this paper. Nevertheless, by calculating the changes in R_1

342 reactions, this study provides a possible explanation for the relatively small decrease in

343 HONO during the epidemic period.

344 **4. Conclusions**

345 Elevated NH_3 concentration was observed during the COVID-19 pandemic at both

346 urban and rural sites in China. In addition to the rise in T and decrease in RH during the

347 COVID-19 pandemic, which favored the conversion of NH_4^+ to NH_3, the significant

348 decrease in sulfate and nitrate concentrations led to the decline in Required-NH_x and

349 was beneficial to the particle-phase NH_4^+ portioning to gas-phase NH_3. Furthermore,

350 under the environmental conditions of increased anion concentrations (especially

351 sulfate and nitrate) and increased cation concentrations, the pH values increased by 0.5

and 0.3 at U-ZK and R-PY sites increased during the pandemic, respectively. Consequently, the high pH values accelerated the formation rate of HONO through the oxidation-reduction reaction of NO_2 with SO_2 (an increase of 58% at U-ZK and 59% at R-PY, respectively), partially compensating for the decrease in HONO concentration caused by the decline in vehicle emissions, NO_2 and NO_3^- concentrations during the COVID-19 pandemic.

5. Implications

HONO plays a crucial role as a precursor to OH radicals in the tropospheric atmosphere (Xue, 2022). There have been significant observations of high HONO concentrations in urban areas during the daytime, leading to a growing interest in understanding its sources in atmospheric chemistry (Jiang et al., 2022;Xu et al., 2019). The heterogeneous reaction mechanism of NO_2 on aerosol surfaces is currently the focus of research on HONO sources, particularly in regions with elevated levels of atmospheric particulate matter, where it could potentially become a major contributor to HONO production (Zhang et al., 2022;Liao et al., 2021b). One of the pathways for heterogeneous reactions on aerosol surfaces is the redox reaction of NO_2 with SO_2. However, the significance of this reaction in HONO production in the real atmosphere is often overlooked, as it relies on the high pH of aerosols (Ge et al., 2019). In recent years, there has been increasing attention on the enhancing effect of NH_3 on the redox reaction, with laboratory experiments demonstrating its ability to generate substantial amounts of HONO (Ge et al., 2019). This study highlights the importance of this

373   reaction based on actual atmospheric observations. Furthermore, numerous studies

374   have indicated that if control over NH_3 emissions continues to relax while SO_2 and NO_2

375   emissions decrease, the particle pH in future China is expected to rise steadily (Xie et

376   al., 2020;Song et al., 2019;Wang et al., 2020). Consequently, the redox reaction of NO_2

377   with SO_2 could become a significant source of HONO in China. Therefore, it is crucial

378   to coordinate the control of SO_2, NO_x, and NH_3 emissions to avoid a rapid increase in

379   the particle pH.

380

Data availability: All the data presented in this article can be accessed through

https://zenodo.org/records/10273539. (Zhang, 2023).

383

Author contributions. XZ Data Curation, Writing - Original Draft, Visualization.

LW, NW, SM, and DZ Investigation, Visualization, Data Curation. DZ, HZ, and MW

Investigation. SW Conceptualization, Data Curation, Supervision. RZ Data Curation,

Funding acquisition. All people are involved in the discussion of the results.

388

Competing interest. The authors declare no competing financial interest.

390

Acknowledgments. This work was supported by the China Postdoctoral Science

Foundation (2023M733220), the Zhengzhou $PM_{2.5}$ and O_3 Collaborative Control and

Monitoring Project (20220347A), and the National Key Research and Development

Program of China (No. 2017YFC0212403).

References

Alicke, B.: OH formation by HONO photolysis during the BERLIOZ experiment, J. Geophy. Res., 108, 8247, https://doi.org/10.1029/2001JD000579, 2003.

Atkinson, R., Baulch, D.L., Cox, R.A., Crowley, J.N., Hampson, R.F., Hynes, R.G., Jenkin, M.E., and Rossi, M. J., Troe, J.: Evaluated kinetic and photochemical data for atmospheric chemistry: volume I - gas phase reactions of O_x, HO_x, NO_x and SO_x species., Atmos. Chem. Phys., 4,1461–1738, https://doi.org/10.5194/acp-4-1461-2004, 2004.

Bougiatioti, A., Nikolaou, P., Stavroulas, I., Kouvarakis, G., Weber, R., Nenes, A., Kanakidou, M., and Mihalopoulos, N.: Particle water and pH in the eastern Mediterranean: source variability and implications for nutrient availability, Atmos. Chem. Phys., 16, 4579–4591, https://doi.org/10.5194/acp-16-4579-2016, 2016.

Chang, Y., Zou, Z., Zhang, Y., Deng, C., Hu, J., Shi, Z., Dore, A. J., and Collett, J. L., Jr.: Assessing contributions of agricultural and nonagricultural emissions to atmospheric ammonia in a Chinese megacity. Environ. Sci. Technol., 53, 1822–1833., https://doi.org/10.1021/acs.est.8b05984, 2019.

Chen, X., Walker, J. T., and Geron, C.: Chromatography related performance of the monitor for aerosols and gases in ambient air (MARGA): laboratory and field-based evaluation. Atmos. Meas. Tech., 10, 3893–3908. https://doi.org/10.5194/amt-10-3893-2017, 2017.

Cheng, Y., Zheng, G., Wei, C., Mu, Q., Zheng, B., Wang, Z., Gao, M., Z., Q., He, K., Carmichael, G., Pöschl, U., and Su, and H.: Reactive nitrogen chemistry in aerosol

water as a source of sulfate during haze events in China, Sci. Adv., 2, e1601530., https://doi.org/10.1126/sciadv.1601530, 2019.

Chow, J. C., Lowenthal, D. H., Chen, L. W. A., Wang, X., and Watson, J. G.: Mass reconstruction methods for $PM_{2.5}$: a review, Air Qual. Atmos. Health., 8, 243 – 263, https://doi.org/10.1007/s11869-015-0338-3, 2015.

Ding, J., Zhao, P., Su, J., Dong, Q., Du, X., and Zhang, Y.: Aerosol pH and its driving factors in Beijing, Atmos. Chem. Phys., 19, 7939–7954., https://doi.org/10.5194/acp-19-7939-2019, 2019.

Ellis, R. A., Murphy, J. G., Markovic, M. Z., VandenBoer, T. C., Makar, P. A., Brook, J., and Mihele, C.: The influence of gas-particle partitioning and surface-atmosphere exchange on ammonia during BAQS-Met, Atmos. Chem. Phys., 11, 133–145., https://doi.org/10.5194/acp-11-133-2011, 2011.

Feng, S., Xu, W., Cheng, M., Ma, Y., Wu, L., Kang, J., Wang, K., Tang, A., Collett, J. L., Fang, Y., Goulding, K., Liu, X., and Zhang, F.: Overlooked nonagricultural and wintertime agricultural NH_3 emissions in Quzhou county, north China plain: evidence from ^{15}N-Stable Isotopes. Environ. Sci. Technol. Lett., 9, 127–133, https://doi.org/10.1021/acs.estlett.1c00935, 2022a.

Feng, T., Zhao, S., Liu, L., Long, X., Gao, C., and Wu, N.: Nitrous acid emission from soil bacteria and related environmental effect over the North China Plain, Chemos., 287, https://doi.org/10.1016/j.chemosphere.2021.132034, 2022b.

Fountoukis, C., Nenes, A.: ISORROPIA II: a computationally efficient thermodynamic equilibrium model for K^+-Ca^{2+}-Mg^{2+}-NH_4^+-Na^+-SO_4^{2-}-NO_3^--Cl^--H_2O aerosols. Atmos. Chem. Phys., 7, 4639–4659, https://doi.org/10.5194/acp-7-4639-2007,

2007.

Ge, S., Wang, G., Zhang, S., Li, D., and Zhang, H.: Abundant NH_3 in China enhances atmospheric HONO production by promoting the heterogeneous reaction of SO_2 with NO_2. Environ. Sci. Technol., 53, 14339–14347, https://doi.org/10.1021/acs.est.9b04196, 2019.

Gong, L., Lewicki, R., Griffin, R. J., Flynn, J. H., Lefer, B. L., and Tittel, F. K.: Atmospheric ammonia measurements in Houston, TX using an external-cavity quantum cascade laser-based sensor, Atmos. Chem. Phys., 11, 9721–9733, https://doi.org/10.5194/acp-11-9721-2011, 2011.

Gu, M., Pan, Y., Walters, W. W., Sun, Q., Song, L., Wang, Y., Xue, Y., and Fang, Y.: ehicular emissions enhanced ammonia concentrations in winter mornings: insights from diurnal nitrogen isotopic signatures. Environ. Sci. Technol., 56, 1578–1585, https://doi.org/10.1021/acs.est.1c05884, 2022.

Gunthe, S. S., Rose, D., Su, H., Garland, R. M., Achtert, P., Nowak, A., Wiedensohler, A., Kuwata, M., Takegawa, N., Kondo, Y., Hu, M., Shao, M., Zhu, T., Andreae, M. O., and Pöschl, U.: Cloud condensation nuclei (CCN) from fresh and aged air pollution in the megacity region of Beijing, Atmos. Chem. Phys., 11, 11023–11039, https://doi.org/10.5194/acp-11-11023-2011, 2011.

Han, S., Hong, J., Luo, Q., Xu, H., Tan, H., Wang, Q., Tao, J., Zhou, Y., Peng, L., He, Y., Shi, J., Ma, N., Cheng, Y., and Su, H.: Hygroscopicity of organic compounds as a function of organic functionality, water solubility, molecular weight, and oxidation level, Atmos. Chem. Phys., 22, 3985–4004, https://doi.org/10.5194/acp-22-3985-2022, 2022.

463   Haskins, J. D., Jaeglé, L., Shah, V., Lee, B. H., Lopez‐Hilfiker, F. D., Campuzano‐

464   Jost, P., Schroder, J. C., Day, D. A., Guo, H., Sullivan, A. P., Weber, R., Dibb, J.,

465   Campos, T., Jimenez, J. L., Brown, S. S., and Thornton, J. A.: Wintertime gas‐

466   particle partitioning and speciation of inorganic chlorine in the lower troposphere

467   over the northeast united states and coastal ocean, J. Geophys. Res.: Atmos., 123,

468   https://10.1029/2018jd028786, 2018.

469   Huang, X., Ding, A., Gao, J., Zheng, B., Zhou, D., Qi, X., Tang, R., Wang, J., Ren, C.,

470   Nie, W., Chi, X., Xu, Z., Chen, L., Li, Y., Che, F., Pang, N., Wang, H., Tong, D.,

471   Qin, W., Cheng, W., Liu, W., Fu, Q., Liu, B., Chai, F., Davis, S. J., Zhang, Q., and

472   He, K.: Enhanced secondary pollution offset reduction of primary emissions

473   during COVID-19 lockdown in China, Natl. Sci. Rev., 8, nwaa137,

474   https://doi.org/10.1093/nsr/nwaa137, 2021a.

475   Huang, X., Zhang, J., Zhang, W., Tang, G., and Wang, Y.: Atmospheric ammonia and

476   its effect on $PM_{2.5}$ pollution in urban Chengdu, Sichuan Basin, China. Environ.

477   Pollut., 291, 118–195. https://doi.org/10.1016/j.envpol.2021.118195, 2021b.

478   Jiang, Y., Xue, L., Shen, H., Dong, C., Xiao, Z., and Wang, W.: Dominant processes of

479   HONO derived from multiple field observations in contrasting environments.

480   Environ. Sci. Technol. Lett., 9, 258–264,

481   https://doi.org/10.1021/acs.estlett.2c00004, 2022.

482   Kleffmann, J., Gavriloaiei, T., Hofzumahaus, A., Holland, F., Koppmann, R., Rupp, L.,

483   Schlosser, E., Siese, M., and Wahner, A.: Daytime formation of nitrous acid: A

484   major source of OH radicals in a forest, Geophys. Res. Lett., 32,

485   https://doi.org/10.1029/2005gl022524, 2005.

486   Kramer, L. J., Crilley, L. R., Adams, T. J., Ball, S. M., Pope, F. D., and Bloss, W. J.:

487   Nitrous acid (HONO) emissions under real-world driving conditions from vehicles

488   in a UK road tunnel, Atmos. Chem. Phys., 20, 5231–5248,

489   https://doi.org/10.5194/acp-20-5231-2020, 2020.

490   Li, J., An, X., Cui, M., Sun, Z., Wang, C., and Li, Y.: Simulation study on regional

491   atmospheric oxidation capacity and precursor sensitivity, Atmos. Environ., 263,

492   118657, https://doi.org/10.1016/j.atmosenv.2021.118657, 2021a.

493   Li, S., Song, W., Zhan, H., Zhang, Y., Zhang, X., Li, W., Tong, S., Pei, C., Wang, Y.,

494   Chen, Y., Huang, Z., Zhang, R., Zhu, M., Fang, H., Wu, Z., Wang, J., Luo, S., Fu,

495   X., Xiao, S., Huang, X., Zeng, J., Zhang, H., Chen, D., Gligorovski, S., Ge, M.,

496   George, C., and Wang, X.: Contribution of vehicle emission and NO_2 surface

497   conversion to nitrous acid (HONO) in urban environments: implications from tests

498   in a tunnel. Environ. Sci. Technol., 55, 15616–15624,

499   https://doi.org/10.1021/acs.est.1c00405, 2021.

500   Liao, S., Zhang, J., Yu, F., Zhu, M., Liu, J., Ou, J., Dong, H., Sha, Q., Zhong, Z., Xie,

501   Y., Luo, H., Zhang, L., and Zheng, J.: High gaseous nitrous acid (HONO)

502   emissions from light-duty diesel vehicles. Environ. Sci. Technol., 55, 200–208,

503   https://doi.org/10.1021/acs.est.0c05599, 2021.

504   Liu, J., Deng, H., Lakey, P. S. J., Jiang, H., Mekic, M., Wang, X., Shiraiwa, M., and

505   Gligorovski, S.: Unexpectedly high indoor HONO concentrations associated with

506   photochemical NO_2 transformation on glass windows. Environ. Sci. Technol., 54,

507   15680–15688, https://doi.org/10.1021/acs.est.0c05624, 2020a.

508 Liu, M., Song, Y., Zhou, T., Xu, Z., Yan, C., Zheng, M., Wu, Z., Hu, M., Wu, Y., and

509   Zhu, T.: Fine particle pH during severe haze episodes in northern China. Geophys.

510   Res. Lett., 44, 5213–5221, https://doi.org/10.1002/2017gl073210, 2017.

511 Liu, P., Chen, H., Song, Y., Xue, C., Ye, C., Zhao, X., Zhang, C., Liu, J., and Mu, Y.:

512   Atmospheric ammonia in the rural North China Plain during wintertime: variations,

513   sources, and implications for HONO heterogeneous formation. Sci. Total.

514   Environ., 861, 160768, https://doi.org/10.1016/j.scitotenv.2022.160768, 2023.

515 Liu, Y., Ni, S., Jiang, T., Xing, S., Zhang, Y., Bao, X., Feng, Z., Fan, X., Zhang, L., and

516   Feng, H.: Influence of Chinese New Year overlapping COVID-19 lockdown on

517   HONO sources in Shijiazhuang, Sci. Total Environ., 745, 141025,

518   https://doi.org/10.1016/j.scitotenv.2020.141025, 2020b.

519 Liu, Y., Zhang, Y., Lian, C., Yan, C., Feng, Z., Zheng, F., Fan, X., Chen, Y., Wang, W.,

520   Chu, B., Wang, Y., Cai, J., Du, W., Daellenbach, K. R., Kangasluoma, J., Bianchi,

521   F., Kujansuu, J., Petäjä, T., Wang, X., Hu, B., Wang, Y., Ge, M., He, H., and

522   Kulmala, M.: The promotion effect of nitrous acid on aerosol formation in

523   wintertime in Beijing: The possible contribution of traffic-related emissions,

524   Atmos. Chem. Phys., 20, 13023–13040, https://doi.org/10.5194/acp-20-13023-

525   2020, 2020c.

526 Liu, Z., Wang, Y., Costabile, F., Amoroso, A., Zhao, C., Huey, L. G., Stickel, R., Liao,

527   J., and Zhu, T.: Evidence of aerosols as a media for rapid daytime HONO

528   production over China, Environ. Sci. Technol., 48, 13023–13040,

529   https://doi.org/10.1021/es504163z, 2014.

530   Lu, K., Guo, S., Tan, Z., Wang, H., Shang, D., Liu, Y., Li, X., Wu, Z., Hu, M., and

531   Zhang, Y.: Exploring atmospheric free-radical chemistry in China: the self-

532   cleansing capacity and the formation of secondary air pollution, Natl. Sci. Rev., 6,

533   579-594, https://doi.org/10.1093/nsr/nwy073, 2018.

534   Luo, L., Bai, X., Lv, Y., Liu, S., Guo, Z., Liu, W., Hao, Y., Sun, Y., Hao, J., Zhang, K.,

535   Zhao, H., Lin, S., Zhao, S., Xiao, Y., Yang, J., and Tian, H.: Exploring the driving

536   factors of haze events in Beijing during Chinese New Year holidays in 2020 and

537   2021 under the influence of COVID-19 pandemic, Sci. Total Environ., 859,

538   160172, https://doi.org/10.1016/j.scitotenv.2022.160172, 2023.

539   Ma, S.: High-resolution assessment of ammonia emissions in China: Inventories,

540   driving forces and mitigation, Atmos. Environ., 229,

541   https://doi.org/10.1016/j.atmosenv.2020.117458, 2020.

542   McFall, A. S., Edwards, K. C., and Anastasio, C.: Nitrate photochemistry at the air-ice

543   interface and in other ice reservoirs, Environ. Sci. Technol., 52, 5710–5717,

544   https://doi.org/10.1021/acs.est.8b00095, 2018.

545   Meng, Z., Xu, X., Lin, W., Ge, B., Xie, Y., Song, B., Jia, S., Zhang, R., Peng, W., Wang,

546   Y., Cheng, H., Yang, W., and Zhao, H.: Role of ambient ammonia in particulate

547   ammonium formation at a rural site in the North China Plain, Atmos. Chem. Phys.,

548   18, 167–184, https://doi.org/10.5194/acp-18-167-2018, 2018.

549   Meusel, H., Tamm, A., Kuhn, U., Wu, D., Leifke, A. L., Fiedler, S., Ruckteschler, N.,

550   Yordanova, P., Lang-Yona, N., Pöhlker, M., Lelieveld, J., Hoffmann, T., Pöschl,

551   U., Su, H., Weber, B., and Cheng, Y.: Emission of nitrous acid from soil and

552   biological soil crusts represents an important source of HONO in the remote

553   atmosphere in Cyprus, Atmos. Chem. Phys., 18, 799–813,

554   https://doi.org/10.5194/acp-18-799-2018, 2018.

555   Nah, T., Guo, H., Sullivan, A. P., Chen, Y., Tanner, D. J., Nenes, A., Russell, A., Ng, N.

556   L., Huey, L. G., and Weber, R. J.: Characterization of aerosol composition, aerosol

557   acidity, and organic acid partitioning at an agriculturally intensive rural

558   southeastern US site, Atmos. Chem. Phys., 18, 11471–11491, https://10.5194/acp-

559   18-11471-2018, 2018.

560   Oswald, R., Behrendt, T., Ermel, M., Wu, D., Su, H., Cheng, Y., Breuninger, C.,

561   Moravek, A., Mougin, E., Delon, C., Loubet, B., Pommerening-Roser, A., Sorgel,

562   M., Poschl, U., and Hoffmann, T., Andreae, M.O., Meixner, F.X., Trebs, I.: HONO

563   emissions from soil bacteria as a major source of atmospheric reactive nitrogen.,

564   Science, 341, 1233–1235, https://www.science.org/doi/10.1126/science.1242266,

565   2013.

566   Pagsberg, P., Bjergbakke, E., Ratajczak, E., Sillesen, A.: Kinetics of the gas phase

567   reaction OH + NO (+M)⁻ > HONO (+M) and the determination of the UV

568   absorption cross sections of HONO., Chem. Phys. Lett., 272, 383–390,

569   https://doi.org/10.1016/s0009-2614(97)00576-9, 1997.

570   Platt, U., Perner, D., Harris, G. W., Winer, A. M., and Pitts, J. N.: Observations of

571   nitrous acid in an urban atmosphere by differential optical absorption, Nature, 285,

572   312–314, https://doi.org/10.1038/285312a0, 1980.

573   Pye, H. O. T., Nenes, A., Alexander, B., Ault, A. P., Barth, M. C., Clegg, S. L., Collett

574   Jr, J. L., Fahey, K. M., Hennigan, C. J., Herrmann, H., Kanakidou, M., Kelly, J. T.,

575   Ku, I. T., McNeill, V. F., Riemer, N., Schaefer, T., Shi, G., Tilgner, A., Walker, J.

T., Wang, T., Weber, R., Xing, J., Zaveri, R. A., and Zuend, A.: The acidity of atmospheric particles and clouds, Atmos. Chem. Phys., 20, 4809–4888, https://10.5194/acp-20-4809-2020, 2020.

Romer, P. S., Wooldridge, P. J., Crounse, J. D., Kim, M. J., Wennberg, P. O., Dibb, J. E., Scheuer, E., Blake, D. R., Meinardi, S., Brosius, A. L., Thames, A. B., Miller, D. O., Brune, W. H., Hall, S. R., Ryerson, T. B., and Cohen, R. C.: Constraints on aerosol nitrate photolysis as a potential source of HONO and NO_x. Environ. Sci. Technol., 52, 13738–13746, https://doi.org/10.1021/acs.est.8b03861, 2018.

Scharko, N. K., Berke, A. E., and Raff, J. D.: Release of nitrous acid and nitrogen dioxide from nitrate photolysis in acidic aqueous solutions, Environ. Sci. Technol., 48, 11991–12001, https://doi.org/10.1021/es503088x, 2014.

Shi, Q., Tao, Y., Krechmer, J. E., Heald, C. L., Murphy, J. G., Kroll, J. H., and Ye, Q.: Laboratory investigation of renoxification from the photolysis of inorganic particulate nitrate, Environ. Sci. Technol., 55, 854–861, https://doi.org/10.1021/acs.est.0c06049, 2021.

Song, S., Gao, M., Xu, W., Shao, J., Shi, G., Wang, S., Wang, Y., Sun, Y., and McElroy, M. B.: Fine-particle pH for Beijing winter haze as inferred from different thermodynamic equilibrium models, Atmos. Chem. Phys., 18, 7423–7438, https://doi.org/10.5194/acp-18-7423-2018, 2018.

Song, S., Nenes, A., Gao, M., Zhang, Y., Liu, P., Shao, J., Ye, D., Xu, W., Lei, L., Sun, Y., Liu, B., Wang, S., and McElroy, M. B.: Thermodynamic modeling suggests declines in water uptake and acidity of inorganic aerosols in Beijing winter haze

598   events during 2014/2015–2018/2019. Environ. Sci. Technol. Lett., 6, 752–760,

599   https://doi.org/10.1021/acs.estlett.9b00621, 2019.

600   Spataro, F., and Ianniello, A.: Sources of atmospheric nitrous acid: state of the science,

601   current research needs, and future prospects, J. Air. Waste. Manag. Assoc., 64,

602   1232–1250, https://doi.org/10.1080/10962247.2014.952846, 2014.

603   Stieger, B., Spindler, G., van Pinxteren, D., Grüner, A., Wallasch, M., and Herrmann,

604   H.: Development of an online-coupled MARGA upgrade for the 2 h interval

605   quantification of low-molecular-weight organic acids in the gas and particle phases,

606   Atmos. Meas. Tech. 12, 281–298, https://doi.org/10.5194/amt-12-281-2019, 2019.

607   Su, H., Cheng, Y., Oswald, R., Behrendt, T., Trebs, I., Meixner, F.X., Andreae, M.O.,

608   Cheng, P., and Zhang, Y., Poschl, U.: Soil nitrite as a source of atmospheric HONO

609   and   OH   radicals.,   Science.,   333,   1616–1618,

610   https://doi.org/10.1126/science.1207687, 2011.

611   Twigg, M. M., Berkhout, A. J. C., Cowan, N., Crunaire, S., Dammers, E., Ebert, V.,

612   Gaudion, V., Haaima, M., Häni, C., John, L., Jones, M. R., Kamps, B., Kentisbeer,

613   J., Kupper, T., Leeson, S. R., Leuenberger, D., Lüttschwager, N. O. B., Makkonen,

614   U., Martin, N. A., Missler, D., Mounsor, D., Neftel, A., Nelson, C., Nemitz, E.,

615   Oudwater, R., Pascale, C., Petit, J.-E., Pogany, A., Redon, N., Sintermann, J.,

616   Stephens, A., Sutton, M. A., Tang, Y. S., Zijlmans, R., Braban, C. F., and

617   Niederhauser, B.: Intercomparison of in situ measurements of ambient NH_3:

618   instrument performance and application under field conditions, Atmos. Meas.

619   Tech., 15, 6755–6787, https://doi.org/10.5194/amt-15-6755-2022, 2022.

620   Wang, C., Yin, S., Bai, L., Zhang, X., Gu, X., Zhang, H., Lu, Q., and Zhang, R.: High-

621   resolution ammonia emission inventories with comprehensive analysis and

622   evaluation in Henan, China, 2006–2016, Atmos. Environ., 193, 11–23,

623   https://doi.org/10.1016/j.atmosenv.2018.08.063, 2018.

624   Wang, S., Wang, L., Li, Y., Wang, C., Wang, W., Yin, S., and Zhang, R.: Effect of

625   ammonia on fine-particle pH in agricultural regions of China: comparison between

626   urban and rural sites, Atmos. Chem. Phys., 20, 2719–2734,

627   https://doi.org/10.5194/acp-20-2719-2020, 2020.

628   Wang, S., Wang, L., Fan, X., Wang, N., Ma, S., and Zhang, R.: Formation pathway of

629   secondary inorganic aerosol and its influencing factors in Northern China:

630   Comparison between urban and rural sites, Sci. Total Environ., 840,

631   https://doi.org/10.1016/j.scitotenv.2022.156404, 2022.

632   Wang, S., Fan, X., Xu, Y., Zhang, R., and Ren, B.: Insight into the non-linear responses

633   of particulate sulfate to reduced SO_2 concentration: A perspective from the

634   aqueous-phase reactions in a megacity in Northern China, Atmos. Res., 290,

635   https://doi.org/10.1016/j.atmosres.2023.106796, 2023a.

636   Wang, W., Wang, S., Xu, J., Zhou, R., Shi, C., and Zhou, B.: Gas-phase ammonia and

637        $PM_{2.5}$ ammonium in a busy traffic area of Nanjing, China, Environ. Sci. Pollut.

638   Res. Int., 23, 1691–1702, https://doi.org/10.1007/s11356-015-5397-3, 2016.

639   Wang, Y., Jin, X., Liu, Z., Wang, G., Tang, G., Lu, K., Hu, B., Wang, S., Li, G., An, X.,

640   Wang, C., Hu, Q., He, L., Zhang, F., and Zhang, Y.: Progress in quantitative

641   research on the relationship between atmospheric oxidation and air quality, J.

642   Environ. Sci., 123, 350–366, https://doi.org/10.1016/j.jes.2022.06.029, 2023b.

643   Wells, M., Choularton, T. W., and Bower, K. N.: A modelling study of the interaction

644   of   ammonia   with   cloud.,   Atmos.   Environ.,   32,   359–363,

645   https://doi.org/10.1016/s1352-2310(97)00199-4, 1998.

646   Wentworth, G. R., Murphy, J. G., Benedict, K. B., Bangs, E. J., and Collett Jr, J. L.: The

647   role of dew as a night-time reservoir and morning source for atmospheric ammonia,

648   Atmos. Chem. Phys., 16, 7435–7449, https://doi.org/10.5194/acp-16-7435-2016,

649   2016.

650   Wu, C., Lv, S., Wang, F., Liu, X., Li, J., Liu, L., Zhang, S., Du, W., Liu, S., Zhang, F.,

651   Li, J., Meng, J., and Wang, G.: Ammonia in urban atmosphere can be substantially

652   reduced by vehicle emission control: A case study in Shanghai, China, J. Environ.

653   Sci., 126, 754–760, https://doi.org/10.1016/j.jes.2022.04.043, 2023.

654   Xie, Y., Wang, G., Wang, X., Chen, J., Chen, Y., Tang, G., Wang, L., Ge, S., Xue, G.,

655   Wang, Y., and Gao, J.: Nitrate-dominated $PM_{2.5}$ and elevation of particle pH

656   observed in urban Beijing during the winter of 2017. Atmos. Chem. Phys., 20,

657   5019–5033, https://doi.org/10.5194/acp-20-5019-2020, 2020.

658   Xing, L., Fu, T. M., Cao, J. J., Lee, S. C., Wang, G. H., Ho, K. F., Cheng, M. C., You,

659   C. F., and Wang, T. J.: Seasonal and spatial variability of the OM/OC mass ratios

660   and high regional correlation between oxalic acid and zinc in Chinese urban

661   organic   aerosols,   Atmos.   Chem.   Phys.,   13,   4307–4318,

662   https://doi.org/10.5194/acp-13-4307-2013, 2013.

663   Xu, J., Chen, J., Zhao, N., Wang, G., Yu, G., Li, H., Huo, J., Lin, Y., Fu, Q., Guo, H.,

Deng, C., Lee, S.-H., Chen, J., and Huang, K.: Importance of gas-particle partitioning of ammonia in haze formation in the rural agricultural environment, Atmos. Chem. Phys., 20, 7259–7269, https://doi.org/10.5194/acp-20-7259-2020, 2020.

Xu, W., Kuang, Y., Zhao, C., Tao, J., Zhao, G., Bian, Y., Yang, W., Yu, Y., Shen, C., Liang, L., Zhang, G., Lin, W., and Xu, X.: NH_3-promoted hydrolysis of NO_2 induces explosive growth in HONO, Atmos. Chem. Phys., 19, 10557–10570, https://doi.org/10.5194/acp-19-10557-2019, 2019.

Xu, W., Zhao, Y., Wen, Z., Chang, Y., Pan, Y., Sun, Y., Ma, X., Sha, Z., Li, Z., Kang, J., Liu, L., Tang, A., Wang, K., Zhang, Y., Guo, Y., Zhang, L., Sheng, L., Zhang, X., Gu, B., Song, Y., Van Damme, M., Clarisse, L., Coheur, P. F., Collett, J. L., Jr., Goulding, K., Zhang, F., He, K., and Liu, X.: Increasing importance of ammonia emission abatement in $PM_{2.5}$ pollution control. Sci. Bull., 67, 1745–1749, https://doi.org/10.1016/j.scib.2022.07.021, 2022.

Xue, C.: Substantially growing interest in the chemistry of nitrous acid (HONO) in China: current achievements, problems, and future directions. Environ. Sci. Technol., 56, 7375–7377. https://doi.org/10.1021/acs.est.2c02237, 2022.

Ye, C., Zhang, N., Gao, H., and Zhou, X.: Photolysis of particulate nitrate as a source of HONO and NO_x. Environ. Sci. Technol., 51, 6849–6856, https://doi.org/10.1021/acs.est.7b00387, 2017.

Ye, X., Ma, Z., Zhang, J., Du, H., Chen, J., Chen, H., Yang, X., Gao, W., and Geng, F.: Important role of ammonia on haze formation in Shanghai, Environ. Res. Lett., 6,

686   024019, https://doi.org/10.1088/1748-9326/6/2/024019, 2011.

687   Zhang, Q., Liu, P., Wang, Y., Gerorge, C., Chen, T., Ma, S. L., Ren, Y., Mu, Y., Song,

688   M., Herrmann, H., Mellouki, A., Chen, J., Zhao, X., Wang, S., and Y., Z.:

689   Unveiling the underestimated direct emissions of nitrous acid (HONO), Proc. Natl.

690   Acad. Sci. U.S.A., 120, https://doi.org/10.1073/pnas.2302048120, 2023.

691   Zhang, W., Tong, S., Jia, C., Wang, L., Liu, B., Tang, G., Ji, D., Hu, B., Liu, Z., Li, W.,

692   Wang, Z., Liu, Y., Wang, Y., and Ge, M.: Different HONO sources for three layers

693   at the urban area of Beijing. Environ. Sci. Technol., 54, 12870–12880,

694   https://doi.org/10.1021/acs.est.0c02146, 2020a.

695   Zhang, W., Tong, S., Jia, C., Ge, M., Ji, D., Zhang, C., Liu, P., Zhao, X., Mu, Y., Hu, B.,

696   Wang, L., Tang, G., Li, X., Li, W., and Wang, Z.: Effect of different combustion

697   processes on atmospheric nitrous acid formation mechanisms: a winter

698   comparative observation in urban, suburban and rural areas of the North China

699   Plain. Environ. Sci. Technol., 56, 4828–4837,

700   https://doi.org/10.1021/acs.est.1c07784, 2022.

701   Zhang, Y., Liu, X., Fang, Y., Liu, D., Tang, A., and Collett, J. L.: Atmospheric ammonia

702   in Beijing during the COVID-19 outbreak: concentrations, sources, and

703   implications. Environ. Sci. Technol. Lett., 8, 32–38,

704   https://doi.org/10.1021/acs.estlett.0c00756, 2020b.

Figures:

706
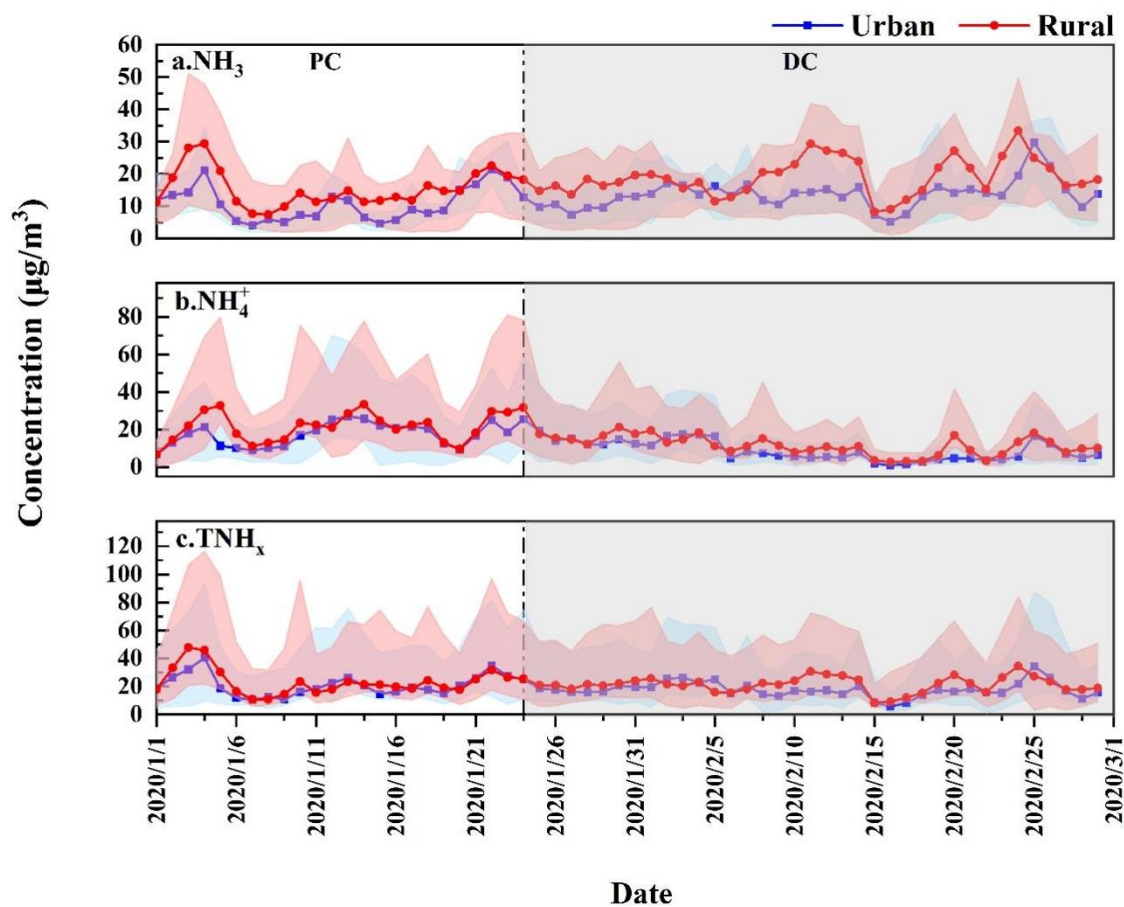
Figure 1. Temporal variations of a. NH_3, b. NH_4^+, and c. TNH_x at the urban and rural

sites before (PC) and during (DC) the COVID-19 outbreak, respectively. The shaded

areas of the curve represent the maximum and minimum values.

710
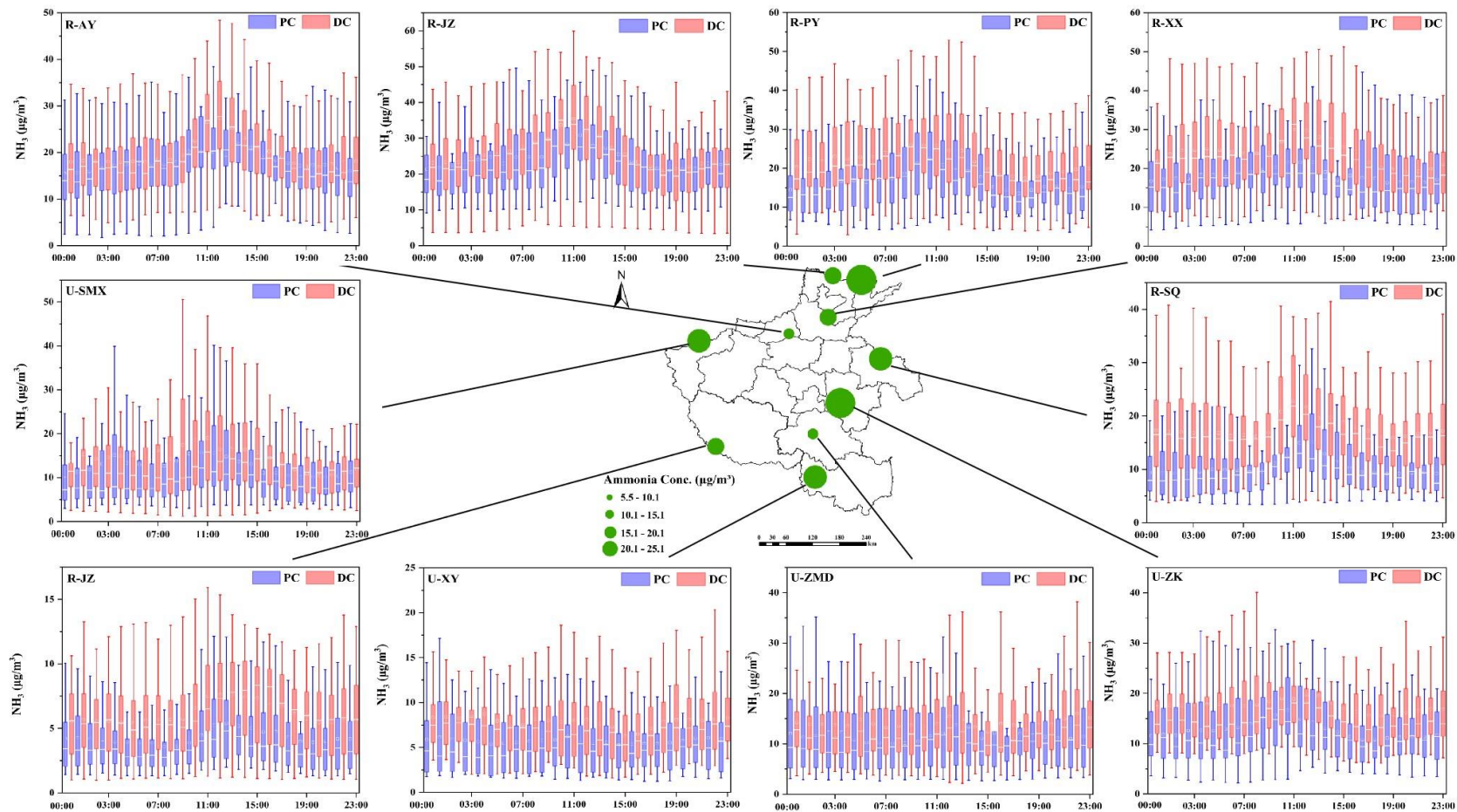
Figure 2. Daily variation of NH$_3$ concentrations at ten sites before (PC) and during (DC) the COVID-19 outbreak. The green dots represent the

location of ten sites and their size represents the concentration of NH$_3$; In each box, the top, middle, and bottom lines represent the 75, 50, and 25

percentiles of statistical data, respectively; the upper and lower whiskers represent the 90 and 10 percentiles of statistical data, respectively.

714
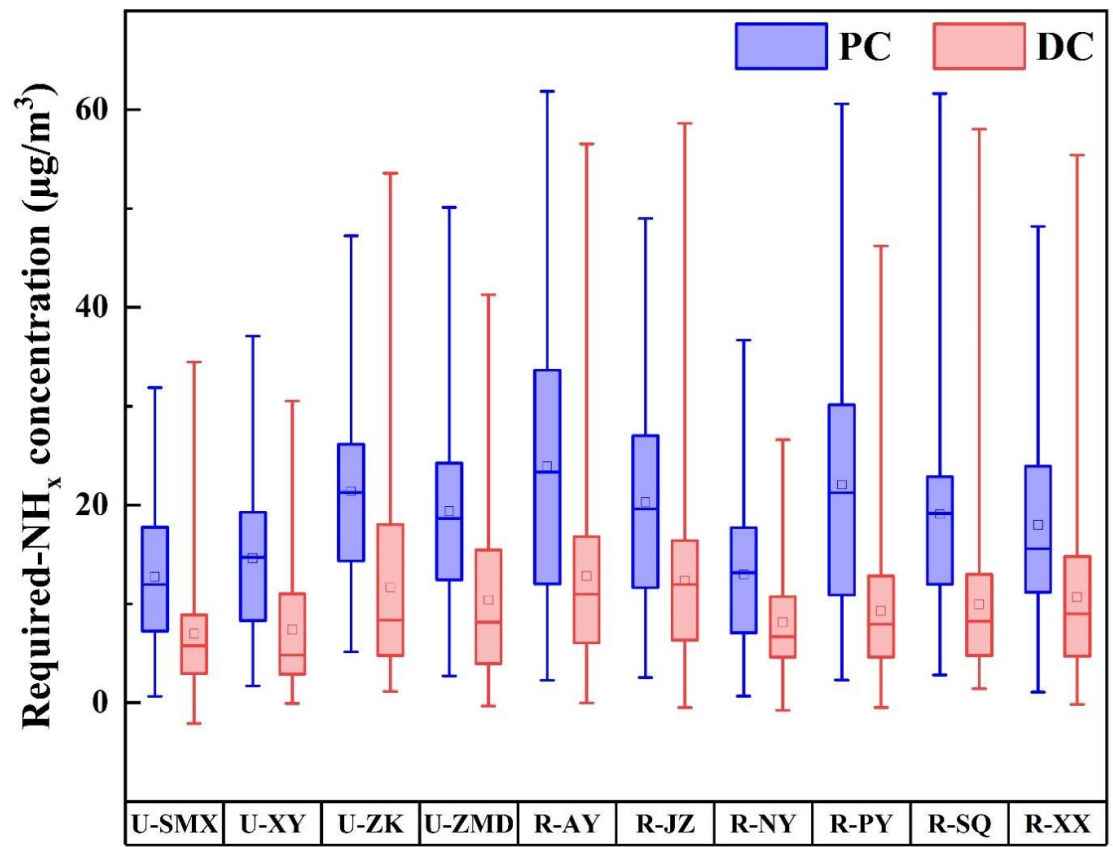
Figure 3. Box diagram of changes in Required-NH$_x$ at ten sites before (PC) and during

(DC) the COVID-19 outbreak. In each box, the top, middle, and bottom lines represent

the 75, 50, and 25 percentiles of statistical data, respectively; the upper and lower

whiskers represent the 90 and 10 percentiles of statistical data, respectively.
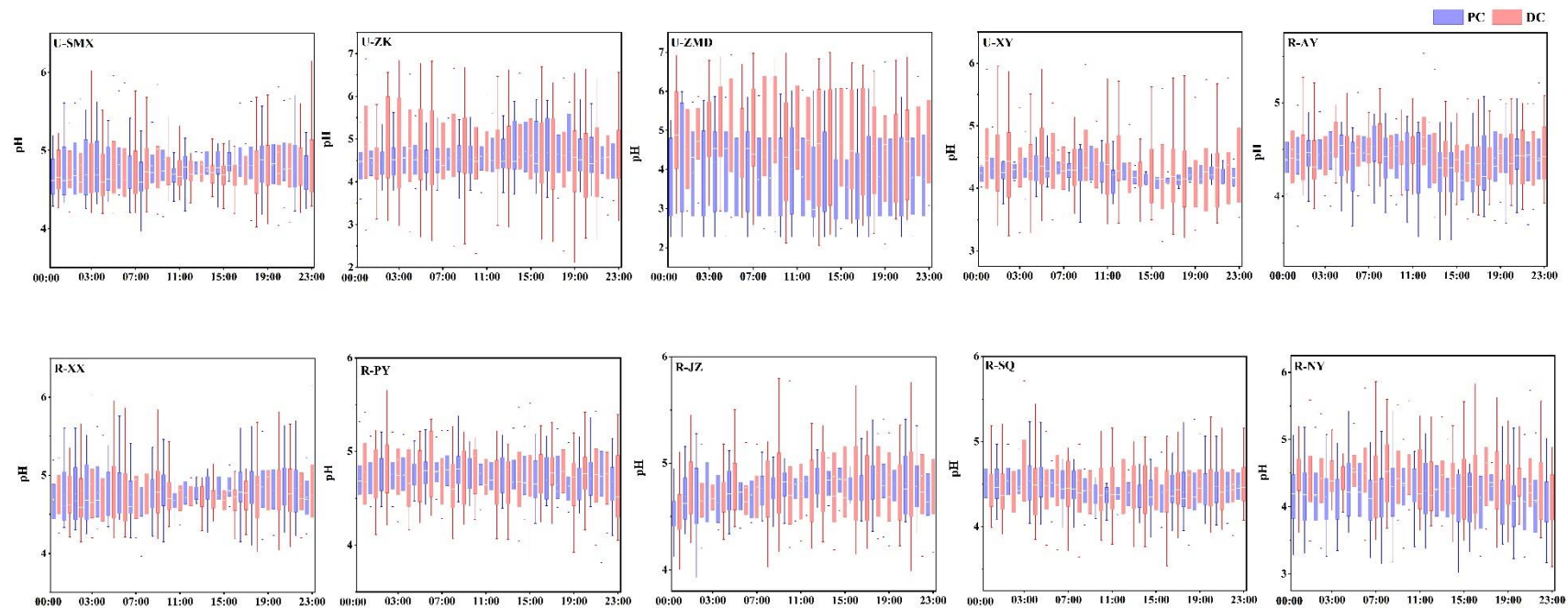
719

720 Figure 4. Diurnal patterns of pH at ten sites before (PC) and during (DC) the COVID-19 outbreak. In each box, the top, middle, and bottom

721 lines represent the 75, 50, and 25 percentiles of statistical data, respectively; the upper and lower whiskers represent the 90 and 10 percentiles of

722 statistical data, respectively.
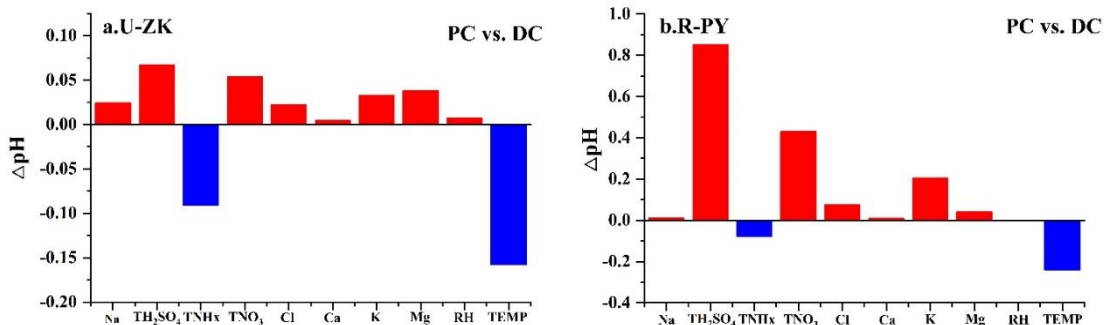
723

724   Figure 5. Changes of pH (ΔpH) through the sensitivity tests (Figure S5 and S6) by

725   changing parameters between PC and DC at the a. U-ZK and b. R-PY sites.
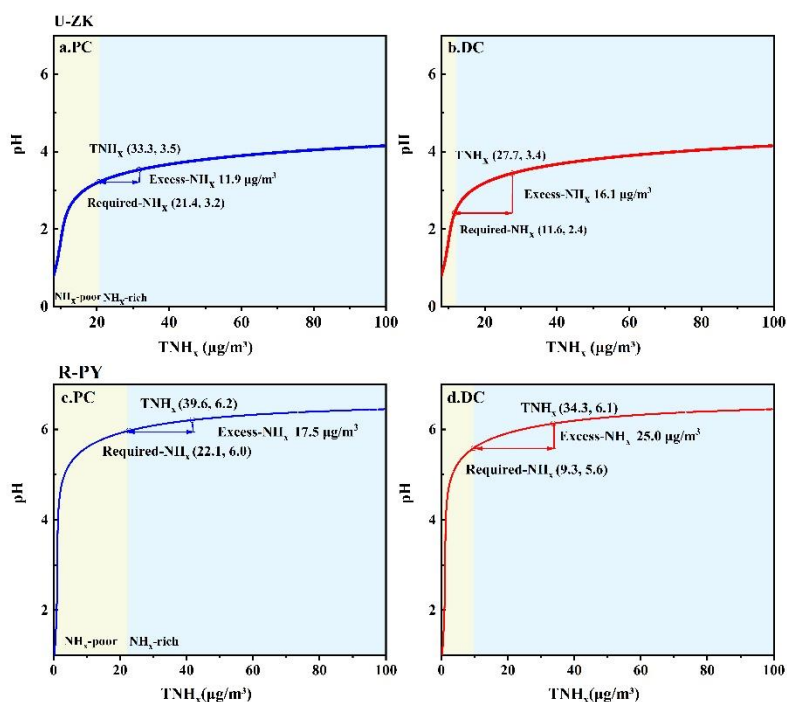
726

727   Figure 6. Particle pH corresponds to increasing TNH_x at U-ZK and R-PY sites to

728   examine the effects of major indicators of NH_3 (i.e., TNH_x, Required-NH_x, and Excess-

729   NH_x) on aerosol acidity. Particle pH was calculated by using a wide range of TNH_x

730   (25–130 μg/m³) and average values of other parameters in PC and DC of U-ZK and R-

731   PY sites. The concentrations of TNH_x, Required-NH_x, and Excess-NH_x with

732   corresponding pH values are marked by a hollow box, hollow circle, and arrow

733   respectively. The yellow and blue background colors correspond to the NH_x-poor and

734   NH_x-rich, respectively.
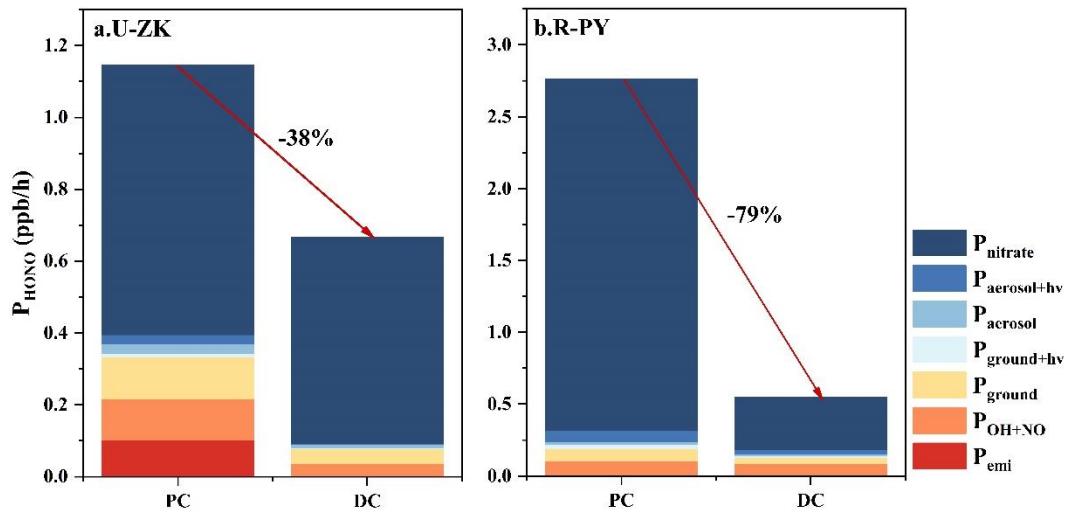
735

736 Figure 7. Comparison of HONO sources at a. U-ZK and b. R-PY sites before (PC) and

737 during (DC) the COVID-19 outbreak. The calculation method can be found in Text S4.

738
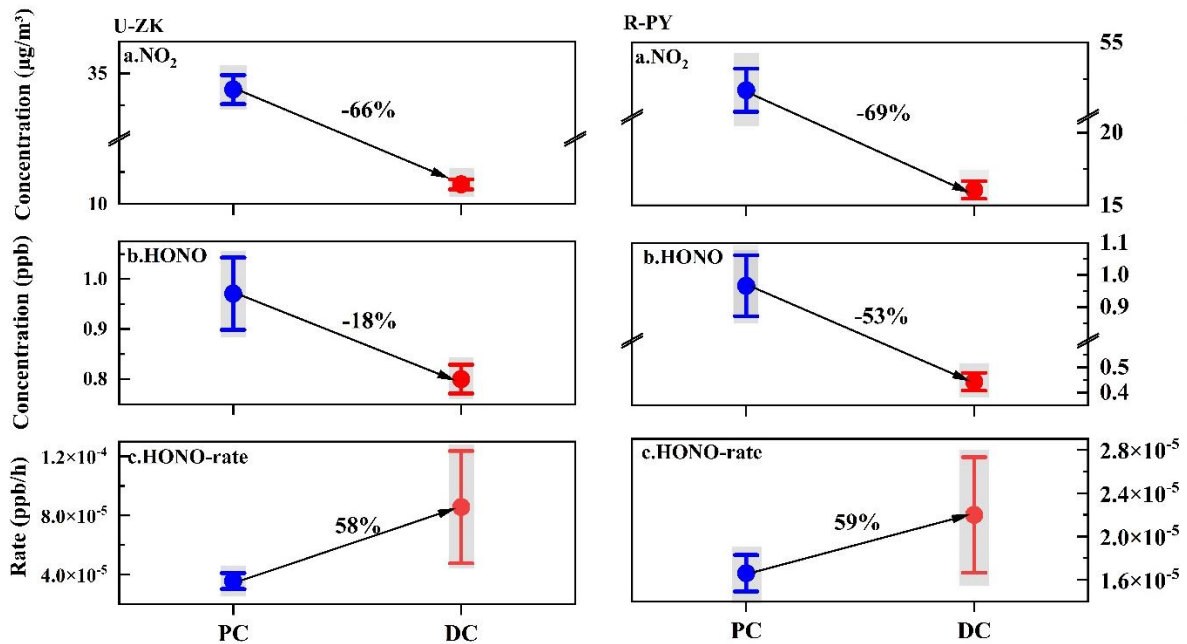
739

740 Figure 8. Decline ratios of a. NO_2, b. HONO concentration, and c. HONO production

741 rate at U-ZK and R-PY sites before (PC) and during (DC) the COVID-19 outbreak. The

742 center point represents the mean value, and the upper and lower whiskers represent the

743 95% confidence interval of the mean. The shadows in the figure represent the

744 uncertainties of NO_2 measurement (±10%), HONO measurement (±20%), and the

745 HONO formation rate of R_1 reaction (−78–123%), respectively.

746

747 **Table:**

748 Table 1. Changes in concentrations (mean ± standard deviation) of NH_3, NH_4^+, and

749 TNH_x at ten sites during entire periods (Average), before (PC), and during (DC) the

750 COVID-19 outbreak.

Sites	Substances	Average (µg/m³)	PC (µg/m³)	DC (µg/m³)
U-SMX	NH_3	13.8 ± 10.8	12.6 ± 10.1	14.5 ± 11.1
	NH_4^+	10.9 ± 7.2	14.2 ± 7.2	8.8 ± 6.5
	TNH_x	22.9 ± 14.1	24.9 ± 14.5	21.7 ± 13.8
U-ZK	NH_3	15.6 ± 8.3	12.7 ± 6.5	17.4 ± 8.8
	NH_4^+	13.6 ± 9.3	19.1 ± 8.4	10.3 ± 8.1
	TNH_x	28.6 ± 13.7	30.9 ± 12.8	27.1 ± 14.0
U-ZMD	NH_3	13.1 ± 8.4	11.6 ± 8.2	14.0 ± 8.4
	NH_4^+	13.9 ± 9.8	19.6 ± 10.3	10.3 ± 7.5
	TNH_x	25.7 ± 14.6	30.3 ± 15.1	22.8 ± 13.5
U-XY	NH_3	7.0 ± 4.3	5.7 ± 4.0	7.9 ± 4.3
	NH_4^+	11.0 ± 7.7	15.4 ± 7.6	8.3 ± 6.5
	TNH_x	17.6 ± 9.8	20.6 ± 10.1	15.7 ± 9.2
R-AY	NH_3	19.0 ± 8.4	17.9 ± 8.3	19.7 ± 8.4
	NH_4^+	19.3 ± 12.9	26.4 ± 13.7	15.0 ± 10.3
	TNH_x	36.6 ± 18.2	41.7 ± 20.4	33.4 ± 16.0
R-XX	NH_3	21.7 ± 10.2	18.1 ± 9.3	23.8 ± 10.1
	NH_4^+	15.9 ± 10.4	20.6 ± 11.0	13.0 ± 8.8
	TNH_x	34.9 ± 17.0	35.1 ± 18.8	34.8 ± 15.8
R-PY	NH_3	19.8 ± 9.4	16.8 ± 8.1	21.7 ± 9.6
	NH_4^+	17.4 ± 11.8	25.3 ± 12.6	12.4 ± 8.0
	TNH_x	35.2 ± 17.8	39.4 ± 19.8	32.6 ± 15.7
R-JZ	NH_3	25.3 ± 11.5	24.1 ± 11.5	25.9 ± 11.4
	NH_4^+	17.3 ± 11.3	22.7 ± 11.6	14.2 ± 9.9
	TNH_x	40.8 ± 20.1	42.9 ± 22.8	33.5 ± 18.2
R-SQ	NH_3	15.0 ± 7.9	10.3 ± 5.2	17.7 ± 7.9
	NH_4^+	13.4 ± 8.5	18.9 ± 8.6	10.3 ± 6.7
	TNH_x	26.3 ± 13.2	25.5 ± 14.0	26.8 ± 12.7
R-NY	NH_3	5.5 ± 3.1	4.3 ± 2.7	6.2 ± 3.2
	NH_4^+	10.2 ± 6.9	13.3 ± 7.2	8.4 ± 6.1
	TNH_x	14.8 ± 8.5	16.0 ± 9.5	14.1 ± 7.8

751
752